



Aspect ratio effect on side and basal melting in fresh water

Dehao Xu¹ , Rui Yang^{1,2} , Roberto Verzicco^{1,3,4}  and Detlef Lohse^{1,5} 

¹Physics of Fluids Department, Max Planck Center for Complex Fluid Dynamics, J.M. Burgers Centre for Fluid Dynamics, University of Twente, Enschede 7500AE, The Netherlands

²Department of Mechanical and Aerospace Engineering, Princeton University, Princeton, NJ 08544, USA

³Dipartimento di Ingegneria Industriale, University of Rome ‘Tor Vergata’, Roma 00133, Italy

⁴Gran Sasso Science Institute – Viale F. Crispi, 767100, L’Aquila, Italy

⁵Max Planck Institute for Dynamics and Self-Organization, Am Faßberg 17, Göttingen 37077, Germany

Corresponding authors: Dehao Xu, d.xu-1@utwente.nl; Detlef Lohse, d.lohse@utwente.nl

(Received 5 November 2024; revised 13 March 2025; accepted 17 March 2025)

The aspect ratio effect on side and basal melting in fresh water is systematically investigated across a range of Rayleigh numbers and ambient temperatures using direct numerical simulations. The side mean melt rate follows a $Ra^{1/4} \gamma^{-3/8}$ scaling relation in the side-melting dominant regime, where Ra is the Rayleigh number, and γ is the width-to-height aspect ratio of the ice block. In the basal-melting dominant regime, the basal mean melt rate follows a $Ra^{1/4} \gamma^{3/8}$ scaling relation at low Rayleigh numbers, but transitions to a $Ra^{1/3} \gamma^{1/2}$ scaling relation at higher Rayleigh numbers. This scaling transition is attributed to the formation of a bottom cavity resulting from flow separation at high Rayleigh numbers. The overall mean melt rate exhibits a non-monotonic dependence on the aspect ratio, driven by the competition between side and basal melting. The proposed theoretical model successfully captures the observed non-monotonic behaviour, and accurately predicts the overall mean melt rate over the considered range of Rayleigh numbers and ambient temperatures, especially in the side- and basal-melting dominant regimes. More specifically, the side, basal and overall mean melt rates follow a linear St scaling relation for ambient temperatures $T_w \geq 15^\circ\text{C}$, with St being the Stefan number (the ratio between sensible heat and latent heat), but deviations from this scaling relation and a non-monotonic dependence on the ambient temperature are observed at lower ambient temperatures, which can be attributed to the density anomaly effect.

Key words: multiphase flow, solidification/melting, sea ice

1. Introduction

The melting process is of critical importance in various geophysical and industrial fields, including the melting of icebergs and ice shelves (Huppert & Turner 1978; Epstein & Cheung 1983; Dutrieux *et al.* 2014; Ristroph 2018), the food industry (Rahman 2020) and the melting of phase-change materials (Dhaidan & Khodadadi 2015). Given the rapid depletion of the Earth's ice reserves (Chen *et al.* 2006; Sutherland *et al.* 2019), understanding the melting behaviour of ice is increasingly crucial in our warming climate. The accelerated loss of icebergs and sea ice floes significantly impacts climate and environmental changes, such as the reduction of the Atlantic meridional overturning circulation (Srokosz *et al.* 2012), the reduction of sea ice cover and thus a loss of albedo (Pistone *et al.* 2014; Jenkins & Dai 2021), and the enhanced drawdown and sequestration of CO₂ (Smith *et al.* 2013; Duprat *et al.* 2016). Consequently, it is essential to improve current climate models to more accurately predict observed changes in ice cover. Enhancing our understanding of ice sheet–ocean interactions on a fundamental level is imperative, as the physical processes governing these interactions remain inadequately understood (Truffe & Motyka 2016; Malyarenko *et al.* 2020; Cenedese & Straneo 2023; Du *et al.* 2024).

The coupling between fluid motions and the evolution of solid boundaries driven by the melting process results in a moving free-boundary problem, i.e. the Stefan problem (Rubinstein 1971). This problem is highly complex since the evolution of the surface forms part of the solution to be determined. During melting, the solid–liquid interface continually recedes due to the heat flux across it, and the meltwater released by the phase change process subsequently alters the temperature field in the surrounding fluid. Temperature changes lead to density variations that drive buoyancy-driven convective flows. While buoyancy-driven convective flows with fixed boundaries are well studied (Bejan 1993; Kadanoff 2001; Ahlers *et al.* 2009; Lohse & Xia 2010; Schlichting & Gersten 2017; Lohse & Shishkina 2023, 2024), the underlying mechanisms governing the interplay between morphology evolution driven by melting, and the dynamics of buoyancy-driven convective flow remain to be developed and explored.

Many previous experimental and numerical studies have investigated the interaction between ice melting and ambient flow at laboratory scales, including dispersed ice melting in flows (Vanier & Tien 1970; Hao & Tao 2002; Hester *et al.* 2021; Weady *et al.* 2022; Yang *et al.* 2024*b*), the influence of convective flows (Davis *et al.* 1984; Dietsche & Müller 1985; Favier *et al.* 2019; Wang *et al.* 2021*a,b*; Yang *et al.* 2023), the impact of shear (Couston *et al.* 2021; Hester *et al.* 2021), and the effect of rotation (Ravichandran & Wettlaufer 2021; Toppaladoddi 2021; Ravichandran *et al.* 2022). Additionally, the melting process in water is notably complex due to the unique effect of temperature on the density of liquid water, which reaches a maximum at approximately 4 °C. This density anomaly leads to distinct regimes of ice morphology and melting rates under varying ambient water temperatures (Wang *et al.* 2021*a*; Weady *et al.* 2022).

Despite extensive investigations into the fundamental mechanisms of the melting process (Dhaidan & Khodadadi 2015; Malyarenko *et al.* 2020; Cenedese & Straneo 2023; Du *et al.* 2024), the effect of geometry on the melt rate has received comparatively less attention. Icebergs and ice floes exhibit significant variations in shape and size, with horizontal extents ranging from several metres to several hundred kilometres (Budd *et al.* 1980; Silva *et al.* 2006; Andres *et al.* 2015; Rackow *et al.* 2017). A limited number of experiments and simulations have shown that the overall melt rate depends on the aspect ratio (Hester *et al.* 2021; Yang *et al.* 2024*a,b*). Hester *et al.* (2021) conducted a comprehensive set of laboratory experiments and numerical simulations to examine the relationship between melt rate and iceberg size and shape under three distinct ambient

velocities. The depth of the ice block was fixed, and its length was varied to explore how the aspect ratio influences the melt rate. They revealed that the geometry significantly affects iceberg melt rates. In their study, the volume of the ice block is altered as the aspect ratio changes. This raises another fundamental question: for the ice blocks with fixed volume, how do the melt rates depend on the aspect ratio? It is essential to maintain a constant initial volume (or area) for the investigation of shape effects. If the initial volumes (or areas) were to vary, then the melt time required to reach a given fraction of the initial volume (or area), as well as the corresponding mean melt rate, would depend on both the initial volume (or area) and the aspect ratio. This interdependence would obscure the isolated influence of aspect ratio on the melting dynamics. To address this, Yang *et al.* (2024b) investigated the influence of the initial aspect ratio on the melting dynamics of an elliptical ice block immersed in a uniform external flow. They found that the shape of the ice block strongly affects the melt rate, and the aspect ratio corresponding to the slowest melt rate varies with the strength of the external flow. Furthermore, Yang *et al.* (2024a) studied the effect of the initial aspect ratio on the melting dynamics of an elliptical shape of ice immersed in quiescent fresh water, where natural convection driven by thermal buoyancy governs the flow. They observed a non-monotonic relationship between the melt rate and the initial aspect ratio, with circular shapes not exhibiting the slowest melt rate in quiescent fresh water. They also proposed a theoretical model to predict the mean melt rate. However, their model differs from the results of direct numerical simulations and fails to capture the non-monotonic dependence of the melt rate on the initial aspect ratio. This highlights the need for an improved theoretical model capable of accurately predicting the non-monotonic relationship between the initial aspect ratio and melt rate. Moreover, the neglect of the aspect ratio effect in current climate models emphasises the necessity of including this factor to more accurately predict iceberg melt rates.

For rectangular ice blocks with a fixed volume (or area), an increase in the initial aspect ratio reduces the surface area of the side walls while increasing the surface area of the basal walls. As a result, the side melt rate is expected to decrease, whereas the basal melt rate should increase with increasing initial aspect ratio. Thus the non-monotonic dependence of the overall melt rate on the initial aspect ratio can be attributed to the competition between side and basal melting. To quantify this non-monotonic behaviour, it is logical to first investigate the theoretical scaling relations for the side and basal melt rates as a function of the initial aspect ratio separately. These scaling relations can subsequently be integrated to develop a theoretical model for predicting the overall melt rate. Such an approach is extendable to geophysical icebergs. If the scaling relations for the side and basal melt rates of geophysical icebergs can be determined or extrapolated, then it becomes possible to estimate their overall melt rate through these scaling relations.

In this study, we numerically and theoretically investigate the influence of the initial aspect ratio on both side and basal melting of a rectangular ice block with fixed volume (or area) in quiescent fresh water through direct numerical simulations. We propose theoretical scaling relations to characterise the effect of the initial aspect ratio on the side and basal melt rates. Additionally, we introduce a comprehensive theoretical model that correlates the overall melt rate with the initial aspect ratio, derived from the individual scaling relations for side and basal melt rates. Our numerical results demonstrate that the proposed theoretical scaling relations and model can accurately predict the effect of the initial aspect ratio on the side, basal and overall melt rates across varying Rayleigh numbers and ambient temperatures.

The paper is organised as follows. In § 2, we detail the governing equations, control parameters and numerical methods employed in the simulations. Section 3 presents the effect of aspect ratio on side, basal and overall melt rates across varying Rayleigh numbers

with a constant ambient temperature. In § 4, we examine the impact of aspect ratio on side, basal and overall melt rates for different ambient temperatures, while maintaining a fixed Rayleigh number. Finally, we provide conclusions and an outlook in § 5.

2. Numerical method and set-up

In the present study, we rely on the phase field method (Hester *et al.* 2020) to simulate the melting process of a solid in fresh water. This method has been validated extensively and employed in numerous previous investigations (Favier *et al.* 2019; Couston *et al.* 2021; Hester *et al.* 2021; Liu *et al.* 2021; Yang *et al.* 2023, 2024a,b). The phase field variable ϕ is integrated in both time and space, transitioning smoothly from value 1 in the solid phase to 0 in the liquid phase, with the interface defined at $\phi = 1/2$. The governing equations, under the incompressibility condition $\nabla \cdot \mathbf{u} = 0$, are

$$\frac{\partial \mathbf{u}}{\partial t} + \mathbf{u} \cdot \nabla \mathbf{u} = -\frac{\nabla p}{\rho_0} + \nu \nabla^2 \mathbf{u} - \frac{g\rho'}{\rho_0} \mathbf{e}_y - \frac{\phi \mathbf{u}}{\eta}, \quad (2.1)$$

$$\frac{\partial T}{\partial t} + \mathbf{u} \cdot \nabla T = \kappa \nabla^2 T + \frac{\mathcal{L}}{c_p} \frac{\partial \phi}{\partial t}, \quad (2.2)$$

$$\frac{\partial \phi}{\partial t} = C \nabla^2 \phi - \frac{C}{\varepsilon^2} \phi (1 - \phi) \left(1 - 2\phi + \frac{\varepsilon}{\Gamma} (T - T_m) \right). \quad (2.3)$$

Here, \mathbf{u} denotes the velocity field, $\rho' = \rho - \rho_0$ is the fluctuating density from a reference value ρ_0 , p is the kinematic pressure, T is the temperature, $T_m = 0^\circ\text{C}$ is the equilibrium melting temperature, ν is the kinematic viscosity, g represents gravitational acceleration in the vertical direction \mathbf{e}_y , κ is the thermal diffusivity, \mathcal{L} is the latent heat, and c_p is the specific heat capacity. The density anomaly of water near 4°C is incorporated using the relation

$$\rho = \rho_0 (1 - \beta |T - T_{\max}|^q), \quad (2.4)$$

where $\beta = 9.3 \times 10^{-6} (\text{K})^{-q}$ is the generalised thermal expansion coefficient, with the exponent $q = 1.895$ and $T_{\max} = 4^\circ\text{C}$ (Gebhart & Mollendorf 1977; Wang *et al.* 2021a; Yang *et al.* 2024a).

The phase field model employed in this study follows the formulation of Hester *et al.* (2020) and properly reflects the Gibbs–Thomson effect (Hester *et al.* 2020). The symbols ε , η , C and Γ are the parameters of the phase field model, which can be explained as follows. The parameter ε measures the diffuse interface thickness and is set equal to the grid spacing following the convergence tests in Favier *et al.* (2019). The limit $\varepsilon \rightarrow 0$ leads to the exact Stefan boundary condition for temperature at the liquid–solid interface:

$$\mathcal{L}u_n = c_p \kappa \left(\frac{\partial T^{(s)}}{\partial n} - \frac{\partial T^{(l)}}{\partial n} \right), \quad (2.5)$$

where u_n is the normal velocity of the interface between the solid and liquid phases, n represents the normal direction of the interface, and the superscripts (s) and (l) denote the solid and liquid phases, respectively. The penalty parameter η is used to decay the velocity to zero in the solid phase, and is set to equal the time step (Hester *et al.* 2020). Additionally, a direct forcing method is employed to set the velocity to zero for $\phi > 0.9$ to prevent spurious motions in the solid phase (Howland 2022). The diffusivity C is defined as $C = 6\Gamma\kappa/(5\varepsilon\mathcal{L})$, where Γ is the surface energy coefficient related to the Gibbs–Thomson effect (Hester *et al.* 2020; Howland 2022). In this study, we set $C = 1.2\kappa$ and

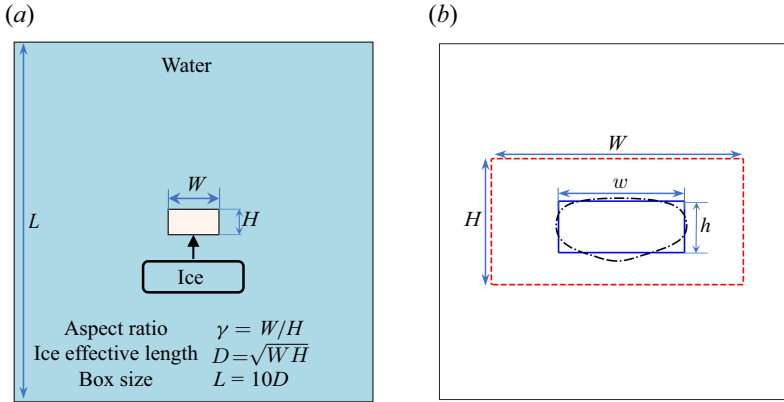


Figure 1. (a) The schematic of the simulation set-up. (b) Illustration depicting the procedure for calculating the side and basal mean melt rates. The red dashed rectangle represents the initial shape of the ice block. The black dash-dotted contour indicates the ice shape at the point when $V_m = 80\%$ of the initial area (volume) of the ice block has melted in 2-D (3-D) simulations. The blue solid rectangle represents the corresponding equivalent ice rectangle.

$\varepsilon \Delta / \Gamma = 10$, where Δ is the initial temperature difference between the ambient water and the ice. Further details and validations of the phase field method can be found in Hester *et al.* (2020) and Howland (2022).

In the simulations, an ice block with an initial cross-sectional area $A_0 = WH$ is placed at the centre of a square box, as depicted in figure 1(a), where W and H represent the initial width and height of the ice block, respectively. The box size L is set to $L = 10D$, where $D = \sqrt{WH}$ is the effective length of the ice block. As confirmed in Appendix A, the computational domain employed in this study is sufficiently large to ensure that the influence of the side walls on the results is negligible.

Simulations are performed using the second-order staggered finite difference code AFiD, which has been validated extensively and used to study a wide range of convection problems (Verzicco & Orlandi 1996; Ostilla-Mónico *et al.* 2015; van der Poel *et al.* 2015), including phase change problems (Liu *et al.* 2021; Yang *et al.* 2023, 2024a,b). The system is governed by four dimensionless control parameters, namely the Rayleigh number Ra , the Prandtl number Pr , the Stefan number St , and the aspect ratio of the initial ice shape γ :

$$Ra = \frac{g\beta\Delta^q D^3}{\nu\kappa}, \quad Pr = \frac{\nu}{\kappa}, \quad St = \frac{c_p\Delta}{\mathcal{L}}, \quad \gamma = \frac{W}{H}. \quad (2.6)$$

Here, $\Delta = T_w - T_i$ is the initial temperature difference between the ambient water and the ice, where T_w is the initial temperature of the ambient water and $T_i = 0^\circ\text{C}$ is the temperature of the ice. Both two-dimensional (2-D) and three-dimensional (3-D) simulations are performed to examine the effect of aspect ratio on the side, basal and overall melting. In the 3-D simulations, the depth of the ice block is set equal to L . All boundaries of the square box are adiabatic, with no-slip conditions for the velocity fields.

Since the initial cross-sectional area of the rectangular ice block remains fixed when varying its aspect ratio, the effective length D serves as a representative measure of the initial cross-sectional area, while the aspect ratio γ characterises the shape of the ice block. These two governing parameters provide a more suitable description of the system than using the height H and width W , as in the present study, H and W cannot be varied independently; rather, they are intrinsically linked. Specifically, their values are determined

by the effective length of the ice block D (i.e. the Rayleigh number Ra) and the aspect ratio γ via the relations $H = D/\sqrt{\gamma}$ and $W = D\sqrt{\gamma}$.

Due to the extensive parameter space, some control parameters are fixed to ensure the feasibility of this study. The Prandtl number is fixed at $Pr = 7$. In § 3, the initial temperature of the surrounding water is fixed at $T_w = 20^\circ\text{C}$, resulting in a Stefan number $St = 0.25$. The simulations explore a range $1.82 \times 10^4 \leq Ra \leq 7.49 \times 10^7$, corresponding to the effective ice dimension $5 \leq D \leq 80$ mm. However, in § 4, also the impact of the initial temperature of the surrounding water on the melt rates is investigated at a fixed Rayleigh number $Ra = 1.46 \times 10^5$. The simulations cover a parameter range $4^\circ\text{C} \leq T_w \leq 20^\circ\text{C}$, corresponding approximately to the Stefan number $0.05 \leq St \leq 0.25$. Additionally, the simulations encompass a range $0.2 \leq \gamma \leq 5.0$ to investigate the aspect ratio effect on the side, basal and overall melt rates.

Given the highly demanding resolution required to resolve the thin ice–water interface in the phase field, the multiple-resolution strategy (Ostilla-Mónico *et al.* 2015) is applied for the phase field. For 2-D simulations, an $N \times N$ uniform mesh is used for the velocity and temperature fields, and a $3N \times 3N$ refined uniform mesh is applied for the phase field, where N increases from 320 to 5120 as the Rayleigh number increases from 1.82×10^4 to 7.49×10^7 . Grid convergence tests for the 2-D simulations are presented in Appendix A. Due to the high computational cost of the 3-D simulations, only five 3-D cases were performed, namely at $Ra = 1.82 \times 10^4$ with $\gamma = 0.2, 0.6, 1, 3, 5$, in order to confirm that the qualitative behaviour observed in the 2-D simulations is consistent with that of the 3-D simulations. An $N \times N \times N$ uniform mesh is employed for the velocity and temperature fields, and a $3N \times 3N \times 3N$ refined uniform mesh is applied for the phase field in the 3-D simulations, where $N = 320$.

3. Effect of Rayleigh number for fixed ambient temperature $T_w = 20^\circ\text{C}$

In this section, the ambient temperature is held constant at $T_w = 20^\circ\text{C}$, leading to a Stefan number $St = 0.25$. The Rayleigh number is varied to investigate its influence on the melt rates. We first propose scaling relations for the side and basal mean melt rates, then construct a theoretical model to estimate the overall mean melt rate.

3.1. Scaling relations of the side and basal mean melt rates

An illustration of the procedure for calculating the side and basal mean melt rates is shown in figure 1(b). The steps to calculate the side and basal mean melt rates can be listed as follows. The black dash-dotted contour shown in figure 1(b) indicates the ice shape at the point when $V_m = 80\%$ of the initial area (volume) of the ice block has melted in 2-D (3-D) simulations. Along this ice contour, the side and basal melt points are defined based on the local slope of the contour points. If the local slope k of a point satisfies $-1 \leq k \leq 1$, then this point is classified as a basal melt point; otherwise, it is considered as a side melt point. The mean locations of the side and basal melt points are then calculated, and an equivalent rectangle of the ice is formed, represented by the blue solid rectangle in figure 1(b), with width w and height h . Finally, the normalised side melt rate \tilde{f}_s and the normalised basal melt rate \tilde{f}_b can be defined as

$$\tilde{f}_s = \frac{W - w}{W\tilde{t}_m}, \quad \tilde{f}_b = \frac{H - h}{H\tilde{t}_m}. \quad (3.1)$$

Here, $\tilde{t}_m = t_m/t_d$, where t_m denotes the time required to melt $V_m = 80\%$ of the initial area (volume) in 2-D (3-D) simulations, and $t_d = D^2/\kappa$ is the thermal diffusion time scale. Additionally, the normalised overall mean melt rate \tilde{f} is defined by $\tilde{f} = 1/\tilde{t}_m = t_d/t_m$.

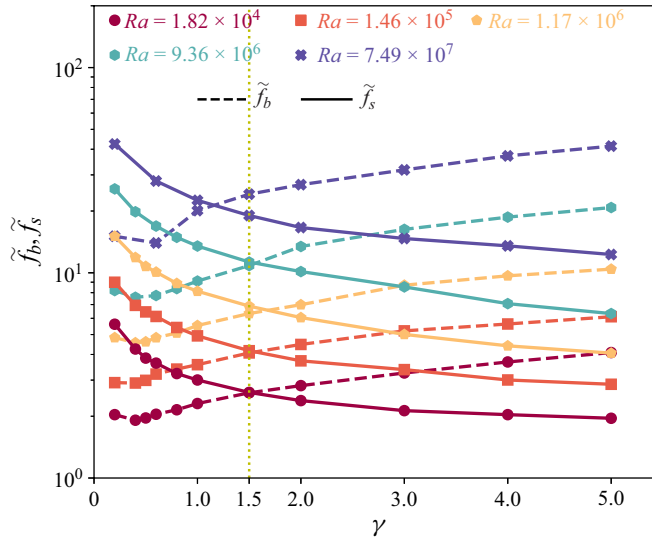


Figure 2. The normalised side mean melt rate \tilde{f}_s and the normalised basal mean melt rate \tilde{f}_b as a function of the aspect ratio γ for different Rayleigh numbers. The symbols connected by solid lines represent the normalised side mean melt rate \tilde{f}_s , and the symbols connected by dashed lines indicate the normalised basal mean melt rate \tilde{f}_b .

It is important to note that different values of the final melt fraction V_m were also tested for calculating the side mean melt rate \tilde{f}_s , the basal mean melt rate \tilde{f}_b , and the overall mean melt rate \tilde{f} . While varying the final melt fraction V_m changes the absolute values of \tilde{f}_s , \tilde{f}_b and \tilde{f} , the overall trend and scaling relations remain consistent, particularly within the range $60\% \leq V_m \leq 80\%$. The temporal evolutions of the side and basal melt rates $\tilde{f}_s(t)$ and $\tilde{f}_b(t)$ are investigated in [Appendix B](#). It is observed that both $\tilde{f}_s(t)$ and $\tilde{f}_b(t)$ remain nearly constant over time, particularly when $60\% \leq V_m \leq 80\%$, indicating that the choice of the final melt fraction V_m within this range does not affect the qualitative results of this study.

The normalised side mean melt rate \tilde{f}_s and the normalised basal mean melt rate \tilde{f}_b as a function of the aspect ratio γ for different Rayleigh numbers are presented in [figure 2](#). The symbols connected by solid lines (for better readability) denote \tilde{f}_s , while the symbols connected by dashed lines represent \tilde{f}_b . As the aspect ratio γ increases, the side mean melt rate \tilde{f}_s decreases, whereas the basal mean melt rate \tilde{f}_b increases. At $\gamma \approx 1.5$, \tilde{f}_s and \tilde{f}_b converge to similar values. For $\gamma \leq 1$, \tilde{f}_s exceeds \tilde{f}_b , indicating a regime where side melting is dominant. Conversely, for $\gamma \geq 2$, \tilde{f}_b surpasses \tilde{f}_s , suggesting a transition to a regime where basal melting becomes dominant.

The normalised side mean melt rate \tilde{f}_s as function of Ra in the side-melting dominant regime ($\gamma \leq 1$) is shown in [figure 3\(a\)](#). It is observed that the side mean melt rate \tilde{f}_s increases with the Rayleigh number. To quantitatively estimate \tilde{f}_s , we consider the thermal Stefan boundary condition (2.5). According to this boundary condition, the dimensionless instantaneous melt velocity \tilde{u}_n is related to the dimensionless instantaneous heat flux Nu and the Stefan number St :

$$\tilde{u}_n = \frac{u_n}{U_0} = -\frac{1}{U_0} \frac{\kappa C_p}{\mathcal{L}} \frac{\partial T}{\partial n} = Nu St \frac{D}{d(t)}, \quad (3.2)$$

where $U_0 = D/t_d$ represents the thermal diffusion velocity scale, $d(t) = \sqrt{A(t)}$ is the effective ice length at time t , $A(t)$ is the area of the ice at time t , and

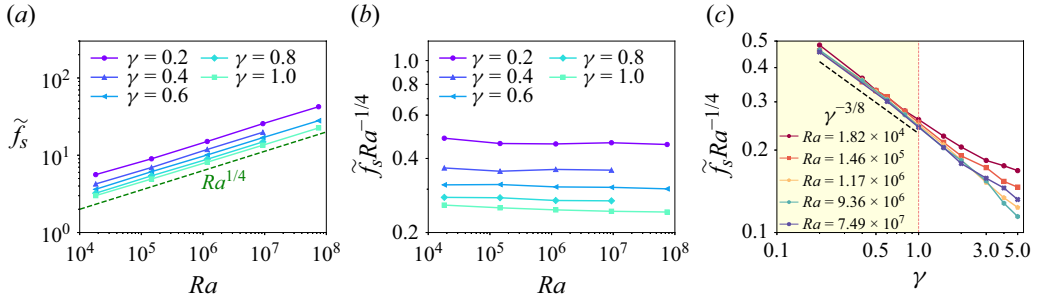


Figure 3. (a) The normalised side mean melt rate \tilde{f}_s as function of Ra in the side-melting dominant regime ($\gamma \leq 1$). (b) The compensated normalised side mean melt rate $\tilde{f}_s Ra^{-1/4}$ as function of Ra in the side-melting dominant regime ($\gamma \leq 1$). (c) The compensated normalised side mean melt rate $\tilde{f}_s Ra^{-1/4}$ as function of γ for different Rayleigh numbers. The yellow region indicates the side-melting dominant regime ($\gamma \leq 1$).

$Nu = -(\partial T / \partial n) / (\Delta / d(t))$ denotes the Nusselt number. Given that the side mean melt rate \tilde{f}_s is equal to the time and space average of \tilde{u}_n along the side surface of the ice, it follows that \tilde{f}_s must be proportional to the time and space average of the dimensionless heat flux \overline{Nu}_s along the side surface, and also proportional to the Stefan number St . In the melting process, the descent of cold meltwater due to thermal buoyancy generates a laminar boundary layer along the side surface of the ice block. Accordingly, \overline{Nu}_s can be estimated by the $\overline{Nu}_s \propto Ra_H^{1/4}$ scaling relation for a laminar boundary layer (Bejan 1993; Grossmann & Lohse 2000, 2001; Holman 2010), where $Ra_H = Ra(H/D)^3$ is the Rayleigh number defined by the cross-sectional height H of the ice, and $H = D/\sqrt{\gamma}$. Therefore, the normalised side mean melt rate \tilde{f}_s should follow the scaling relation

$$\tilde{f}_s \propto Ra^{1/4} \gamma^{-3/8}. \quad (3.3)$$

This scaling relation is fully consistent with the numerical results: in figure 3(b), the compensated normalised side mean melt rate $\tilde{f}_s Ra^{-1/4}$ remains nearly constant across different Rayleigh numbers, confirming the $\tilde{f}_s \propto Ra^{1/4}$ scaling relation in the side-melting dominant regime ($\gamma \leq 1$). Furthermore, figure 3(c) shows that the compensated normalised side mean melt rate $\tilde{f}_s Ra^{-1/4}$ nearly collapses for different Rayleigh numbers in the side-melting dominant regime ($\gamma \leq 1$), and it also follows the $\gamma^{-3/8}$ scaling relation when $\gamma \leq 1$.

The normalised basal mean melt rate \tilde{f}_b as function of Ra in the basal-melting dominant regime ($\gamma \geq 2$) is shown in figure 4(a). The normalised basal mean melt rate \tilde{f}_b also increases as the Rayleigh number increases. Since the basal mean melt rate \tilde{f}_b is equal to the time average of \tilde{u}_n along the basal surface of the ice, according to (3.2), \tilde{f}_b should be proportional to the time and space average of the dimensionless heat flux \overline{Nu}_b along the basal surface, and also proportional to the Stefan number St . For low Rayleigh numbers ($Ra \leq 10^6$), a laminar boundary layer forms around the basal surface of the ice block, with the mean heat flux along the basal surface following the $\overline{Nu}_b \propto Ra_W^{1/4}$ scaling relation for a laminar boundary layer (Bejan 1993; Grossmann & Lohse 2000, 2001; Holman 2010), where $Ra_W = Ra(W/D)^3$ is the Rayleigh number defined by the cross-sectional width W of the ice, and $W = D\sqrt{\gamma}$. Consequently, the normalised basal mean melt rate \tilde{f}_b should follow the scaling relation

$$\tilde{f}_b \propto Ra^{1/4} \gamma^{3/8}. \quad (3.4)$$

This scaling relation is consistent with the numerical results. In figure 4(b), the compensated normalised basal mean melt rate $\tilde{f}_b Ra^{-1/4}$ is almost constant for $Ra \leq 10^6$,

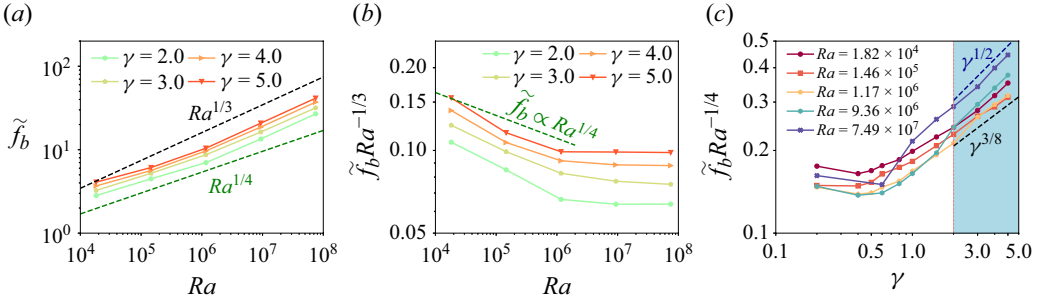


Figure 4. (a) The normalised basal mean melt rate \tilde{f}_b as a function of Ra in the basal-melting dominant regime ($\gamma \geq 2$). (b) The compensated normalised basal mean melt rate $\tilde{f}_b Ra^{-1/4}$ as a function of Ra in the basal-melting dominant regime ($\gamma \geq 2$). (c) The compensated normalised basal mean melt rate $\tilde{f}_b Ra^{-1/4}$ as a function of γ for different Rayleigh numbers. The blue region indicates the basal-melting dominant regime ($\gamma \geq 2$).

particularly for $\gamma \geq 3$ where the basal melt rate significantly exceeds the side melt rate. This confirms that the basal mean melt rate \tilde{f}_b follows an $\tilde{f}_b \propto Ra^{1/4}$ scaling relation in the basal-melting dominant regime ($\gamma \geq 2$) at low Rayleigh numbers. Moreover, figure 4(c) indicates that the compensated normalised basal mean melt rate $\tilde{f}_b Ra^{-1/4}$ adheres to the $\gamma^{3/8}$ scaling relation in the basal-melting dominant regime ($\gamma \geq 2$) when $Ra \leq 10^6$.

For sufficiently high Rayleigh numbers ($Ra > 10^6$), figure 4(b) reveals a transition in the scaling relation of the normalised basal mean melt rate \tilde{f}_b : the scaling relation shifts from $Ra^{1/4}$ to $Ra^{1/3}$ when $Ra > 10^6$. This transition indicates that while the boundary layer remains laminar, the bulk flow around the base of the ice block undergoes a transition from laminar to turbulent, with the mean heat flux along the basal surface following the $\overline{Nu}_b \propto Ra^{1/3}$ scaling relation characteristic of the turbulent bulk flow with a laminar boundary layer (Bejan 1993; Grossmann & Lohse 2000, 2001; Holman 2010). Accordingly, the scaling relation of the normalised basal mean melt rate \tilde{f}_b adjusts to

$$\tilde{f}_b \propto Ra^{1/3} \gamma^{1/2}. \quad (3.5)$$

This scaling relation is consistent with the numerical results shown in figure 4(c), where \tilde{f}_b adheres to the $\gamma^{1/2}$ scaling relation in the basal-melting dominant regime ($\gamma \geq 2$) when $Ra > 10^6$.

The observed scaling transition is due primarily to the formation of a cavity at the bottom of the ice block, as illustrated in figure 5(a–c). Figure 5(a–c) display the instantaneous temperature field for the ice block with various γ values. The formation of the bottom cavity is attributed to the flow separation. At sufficiently high Rayleigh numbers, the descending meltwater along the side surface of the ice block detaches before reaching the base, leading to the development of convection rolls in the bottom region. These convection rolls enhance local mixing, thereby increasing the local heat flux and melt rate, and ultimately contributing to the cavity formation. While the boundary layer along the basal surface remains laminar, the bulk flow in the bottom region transitions to turbulence due to the cavity formation. This triggers the scaling transition of the normalised basal mean melt rate \tilde{f}_b to $Ra^{1/3}$. Additionally, the dimensionless instantaneous heat flux Nu around the ice surface for the ice block with $\gamma = 1.0$ is smaller compared to values for the ice blocks with $\gamma = 0.2$ and $\gamma = 5.0$, implying that the ice block with $\gamma = 1.0$ undergoes a slower melt rate compared to the ice blocks with $\gamma = 0.2$ and $\gamma = 5.0$.

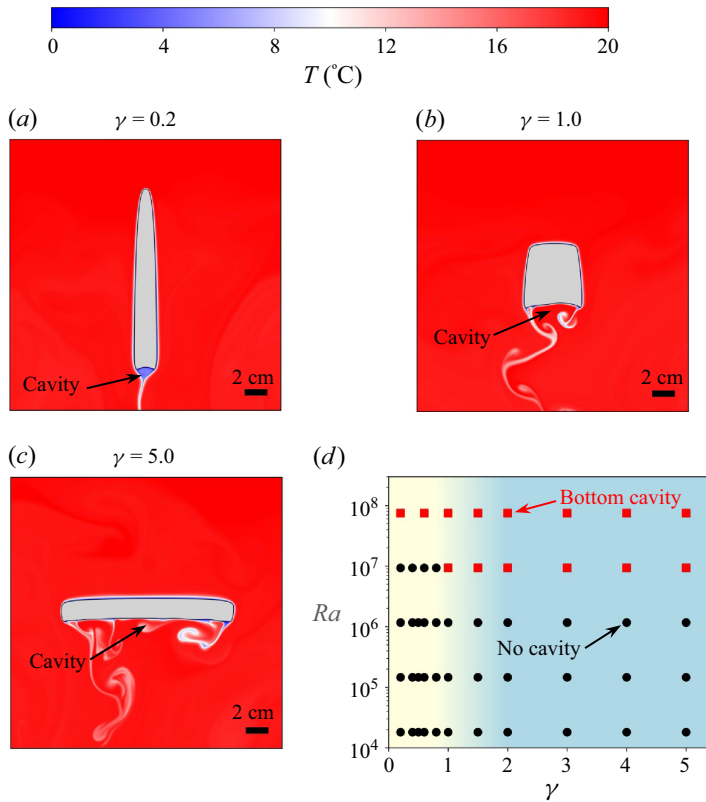


Figure 5. (a–c) The instantaneous temperature field at time $t/t_m = 0.7$ for the ice block with (a) $\gamma = 0.2$, (b) $\gamma = 1.0$ and (c) $\gamma = 5.0$ at $Ra = 7.49 \times 10^7$. The dimensionless instantaneous heat fluxes Nu around the ice surface are 3.47, 2.22 and 3.22 in (a), (b) and (c), respectively. (d) The Ra – γ phase diagram of cavity formation. Black disks and red squares indicate the absence and presence of cavity formation, respectively. The yellow region represents the side-melting dominant regime, and the blue region denotes the basal-melting dominant regime.

Figure 5(d) shows the Ra – γ phase diagram for cavity formation, showing that the bottom cavity forms at either high γ values or high Ra values. At $Ra = 9.36 \times 10^6$, the cavity appears only when $\gamma \geq 1$; however, as the Rayleigh number increases to 7.49×10^7 , the cavity forms for all γ values. The regime transition associated with cavity formation is fully consistent with the corresponding scaling transition in the basal mean melt rate \tilde{f}_b . In the basal-melting dominant regime ($\gamma \geq 2$), the cavity forms when $Ra \geq 9.36 \times 10^6$, leading to the scaling transition of \tilde{f}_b to $Ra^{1/3}$, as shown in figure 4(b). The intensified local melt rate within the cavity significantly enhances the basal mean melt rate \tilde{f}_b , leading to the scaling transition. Due to the observation that the cavity is more readily formed at higher values of γ , it can be inferred that the critical Rayleigh number for the scaling transition of \tilde{f}_b from $Ra^{1/4} \gamma^{3/8}$ to $Ra^{1/3} \gamma^{1/2}$ is smaller for larger γ . To accurately determine the critical Rayleigh number, more data with different Rayleigh numbers and initial aspect ratios are required, which is beyond the scope of the present study.

3.2. Estimation of the overall mean melt rate

Figure 6 presents the compensated normalised overall mean melt rate $\tilde{f} Ra^{-1/4}$ as function of γ for various Rayleigh numbers. Five 3-D simulations were also performed. It is found

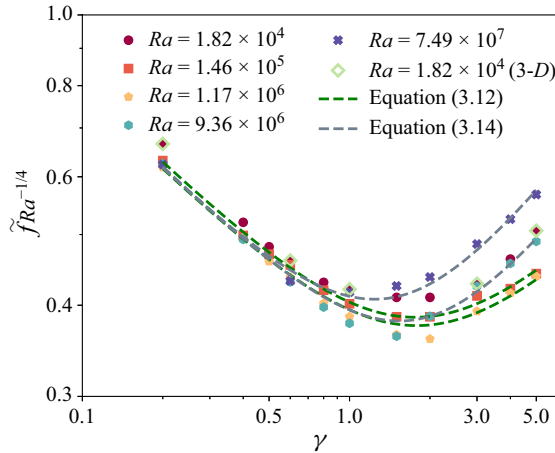


Figure 6. The compensated normalised overall mean melt rate $\tilde{f}Ra^{-1/4}$ as a function of γ for different Rayleigh numbers. The symbols represent the compensated normalised overall mean melt rates $\tilde{f}Ra^{-1/4}$. Two green dashed lines represent the theoretical predictions from (3.12) for the overall mean melt rates $\tilde{f}Ra^{-1/4}$ at $Ra = 1.46 \times 10^5$ and 1.17×10^6 , respectively. Similarly, two grey dashed lines denote the theoretical predictions from (3.14) for the overall mean melt rates $\tilde{f}Ra^{-1/4}$ at $Ra = 9.36 \times 10^6$ and 7.49×10^7 , respectively.

that the overall mean melt rates \tilde{f} in 3-D simulations are nearly identical to those in corresponding 2-D simulations, demonstrating qualitative consistency between 2-D and 3-D results. Due to the more comprehensive data available in 2-D simulations compared to 3-D simulations, however, our analysis focuses primarily on the 2-D simulations.

As the overall mean melt rate \tilde{f} depends on both Ra and γ , the compensated normalised overall mean melt rate $\tilde{f}Ra^{-1/4}$ is used to make the curves for different Ra comparable. The results show that $\tilde{f}Ra^{-1/4}$ collapses at $\gamma \leq 0.6$, especially for $Ra \geq 1.46 \times 10^5$. This phenomenon can be attributed to the dominance of side melting when $\gamma \leq 0.6$, where the side mean melt rate \tilde{f}_s significantly exceeds the basal mean melt rate \tilde{f}_b (figure 2). As figure 3(b) illustrates, the side mean melt rate \tilde{f}_s adheres to the $Ra^{1/4}$ scaling relation in the side-melting dominant regime, leading to the $Ra^{1/4}$ scaling relation for the overall mean melt rate \tilde{f} at $\gamma \leq 0.6$.

The overall mean melt rate exhibits a non-monotonic dependence on the aspect ratio γ : the overall mean melt rate \tilde{f} initially decreases and then increases with increasing γ . This non-monotonic behaviour results from the competition between side and basal melting. For $\gamma \leq 1$, side melting is dominant, and \tilde{f}_s decreases as γ increases (figure 2), leading to a decrease of the overall mean melt rate \tilde{f} with increasing γ . Conversely, for $\gamma \geq 2$, basal melting dominates, and \tilde{f}_b increases as γ increases (figure 2), resulting in an increase of the overall mean melt rate \tilde{f} with increasing γ .

The minimum overall mean melt rate occurs at aspect ratio $\gamma_{min} \approx 2$ when $Ra \leq 1.17 \times 10^6$. The value of γ_{min} deviates from $\gamma = 1$, the configuration where the square-shaped ice block has the smallest perimeter. This reflects that the influence of thermal convection plays a more dominant role in determining the minimum overall melt rate compared to the geometric effect of surface area alone. However, as Ra further increases beyond $Ra \geq 9.36 \times 10^6$, γ_{min} begins to decrease. This decrease of γ_{min} is due mainly to the scaling transition of the basal mean melt rate \tilde{f}_b . For $Ra \geq 9.36 \times 10^6$, the Ra scaling relation of \tilde{f}_b transitions from $Ra^{1/4}$ to $Ra^{1/3}$ (figure 4b), and similarly, the γ scaling relation of \tilde{f}_b shifts from $\gamma^{3/8}$ to $\gamma^{1/2}$ (figure 4c) due to cavity formation. Consequently, the intensity of

the basal mean melt rate \tilde{f}_b is significantly enhanced at higher Rayleigh numbers, causing γ_{min} to decrease at sufficiently high Rayleigh numbers.

Our observations reveal that the aspect ratio γ of the initial ice shape significantly affects the overall mean melt rate, with the ratio of the maximum to the minimum overall mean melt rates at the same Rayleigh number reaching up to 1.7. However, this aspect ratio effect has often been neglected in previous models for estimating the melt rates of icebergs (Weeks & Campbell 1973; Martin & Adcroft 2010), potentially compromising their accuracy. Therefore, it is crucial to incorporate the aspect ratio effect into models for estimating iceberg melt rates to enhance their accuracy.

Based on the previous scaling relations for the side mean melt rate \tilde{f}_s (3.3) and the basal mean melt rate \tilde{f}_b in (3.4) or (3.5), the theoretical model for the overall mean melt rate \tilde{f} can be proposed as follows. As depicted in figure 1(b), the area of the equivalent ice rectangle, represented by the blue solid rectangle with width w and height h , is approximately $1 - V_m$ of the initial area of the ice block shown by the red dashed rectangle, which gives

$$hw = (1 - V_m) HW, \quad (3.6)$$

where $V_m = 80\%$ in this study. Through some rewriting (3.6) becomes

$$V_m - \frac{W - w}{W} - \frac{H - h}{H} + \frac{(W - w)(H - h)}{WH} = 0. \quad (3.7)$$

Upon dividing both sides of (3.7) by \tilde{t}_m^2 , the following equation is obtained:

$$\frac{V_m}{\tilde{t}_m^2} - \frac{W - w}{W\tilde{t}_m^2} - \frac{H - h}{H\tilde{t}_m^2} + \frac{(W - w)(H - h)}{WH\tilde{t}_m^2} = 0. \quad (3.8)$$

By substituting the definitions of the side mean melt rate \tilde{f}_s and the basal mean melt rate \tilde{f}_b from (3.1), as well as the overall mean melt rate $\tilde{f} = 1/\tilde{t}_m$, into (3.8), we obtain

$$V_m \tilde{f}^2 - (\tilde{f}_s + \tilde{f}_b) \tilde{f} + \tilde{f}_s \tilde{f}_b = 0. \quad (3.9)$$

Therefore, the overall mean melt rate \tilde{f} can be expressed as

$$\tilde{f} = \frac{1}{2V_m} \left[(\tilde{f}_s + \tilde{f}_b) + \sqrt{(\tilde{f}_s + \tilde{f}_b)^2 - 4V_m \tilde{f}_s \tilde{f}_b} \right]. \quad (3.10)$$

For low Rayleigh numbers ($Ra \leq 10^6$), the side and basal mean melt rates \tilde{f}_s and \tilde{f}_b can be estimated using the scaling relations given by (3.3) and (3.4), respectively:

$$\tilde{f}_s = a_s \gamma^{-3/8}, \quad \tilde{f}_b = a_{b1} \gamma^{3/8}, \quad (3.11)$$

where a_s and a_{b1} are the coefficients of the scaling relations for the side and basal mean melt rates, respectively. By substituting (3.11) into (3.10), we obtain

$$\tilde{f} \propto \left(\gamma^{-3/8} + a_1 \gamma^{3/8} \right) + \sqrt{\left(\gamma^{-3/8} + a_1 \gamma^{3/8} \right)^2 - 4V_m a_1}, \quad (3.12)$$

where $a_1 = a_{b1}/a_s$ is the ratio of the coefficients of the scaling relations for the side and basal mean melt rates, which can be determined by fitting.

For sufficiently high Rayleigh numbers ($Ra > 10^6$), the side and basal mean melt rates \tilde{f}_s and \tilde{f}_b are estimated by the scaling relations in (3.3) and (3.5), respectively:

$$\tilde{f}_s = a_s \gamma^{-3/8}, \quad \tilde{f}_b = a_{b2} \gamma^{1/2}, \quad (3.13)$$

where a_s and a_{b2} are the coefficients of the scaling relations for the side and basal mean melt rates, respectively. By substituting (3.13) into (3.10), we get

$$\tilde{f} \propto \left(\gamma^{-3/8} + a_2 \gamma^{1/2} \right) + \sqrt{\left(\gamma^{-3/8} + a_2 \gamma^{1/2} \right)^2 - 4V_m a_2 \gamma^{1/8}}, \quad (3.14)$$

where $a_2 = a_{b2}/a_s$ is the ratio of the coefficients of the scaling relations for the side and basal mean melt rates, which can be obtained by fitting from the data.

In order to derive the theoretical model for the overall mean melt rate \tilde{f} in (3.12) and (3.14), an assumption should be made that the scaling relations for \tilde{f}_s and \tilde{f}_b in (3.11) and (3.13) hold for all values of γ . However, this assumption does not apply universally. The scaling relation of \tilde{f}_s is valid only in the side-melting dominant regime, as shown in figure 3(c), while the scaling relation of \tilde{f}_b is accurate only in the basal-melting dominant regime, as depicted in figure 4(c). Therefore, we can infer that the invalidity of the assumption has a small impact on the theoretical model in the side- and basal-melting dominant regimes because the basal mean melt rate \tilde{f}_b is small in the side-melting dominant regime, and the side mean melt rate \tilde{f}_s is small in the basal-melting dominant regime (figure 2). However, the proposed theoretical model obviously fails in the intermediate region where both side and basal mean melt rates significantly contribute to the overall mean melt rate.

Figure 6 illustrates the behaviour of the proposed theoretical model for the overall mean melt rate \tilde{f} in (3.12) and (3.14). Two green dashed lines represent the theoretical predictions from (3.12) for the overall mean melt rates $\tilde{f} Ra^{-1/4}$ at $Ra = 1.46 \times 10^5$ and 1.17×10^6 , respectively. Similarly, two grey dashed lines denote the theoretical predictions from (3.14) for the overall mean melt rates $\tilde{f} Ra^{-1/4}$ at $Ra = 9.36 \times 10^6$ and 7.49×10^7 , respectively. The theoretical model successfully captures the non-monotonic behaviour of \tilde{f} as a function of γ , and accurately estimates \tilde{f} in the regimes where side melting ($\gamma \leq 0.8$) and basal melting ($\gamma \geq 3$) are dominant. However, the model is less accurate in the intermediate region where both side and basal melting have significant contributions to the overall mean melt rate \tilde{f} . It is noted that the overall mean melt rate \tilde{f} is expressed as a function of the initial aspect ratio γ in the proposed theoretical model ((3.12) and (3.14)). However, as demonstrated in Appendix B, the instantaneous equivalent aspect ratio $\gamma(t)$ is changing over time and deviates from its initial value. This discrepancy introduces further inaccuracies in the proposed theoretical model. To enhance the predictive accuracy of the model, future improvements should incorporate the temporal variation of the instantaneous equivalent aspect ratio $\gamma(t)$.

4. Effect of ambient temperature for fixed Rayleigh number $Ra = 1.46 \times 10^5$

In the preceding section, we systematically examined the influence of aspect ratio on the side, basal and overall melting with the ambient temperature maintained at $T_w = 20^\circ\text{C}$. However, the density of water exhibits a non-monotonic dependence on temperature, as described by (2.4). This density anomaly of water near 4°C can give rise to distinct flow regimes and morphological evolutions for varying ambient temperatures (Wang *et al.* 2021a,b; Weady *et al.* 2022). Consequently, in this section, we investigate the impact of the ambient temperature while keeping the Rayleigh number fixed at $Ra = 1.46 \times 10^5$.

The normalised side mean melt rate \tilde{f}_s and the normalised basal mean melt rate \tilde{f}_b as a function of the aspect ratio γ for different ambient temperatures are presented in figure 7. The symbols connected by solid lines represent the normalised side mean melt rate \tilde{f}_s , and the symbols connected by dashed lines indicate the normalised basal mean melt rate \tilde{f}_b . As the aspect ratio γ increases, the side mean melt rate \tilde{f}_s decreases, while the basal mean

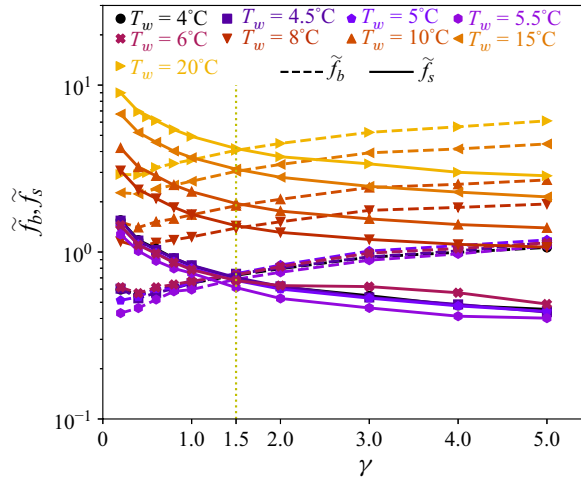


Figure 7. The normalised side mean melt rate \tilde{f}_s and the normalised basal mean melt rate \tilde{f}_b as a function of the aspect ratio γ for different ambient temperatures. The symbols connected by solid lines represent the normalised side mean melt rate \tilde{f}_s , and the symbols connected by dashed lines indicate the normalised basal mean melt rate \tilde{f}_b .

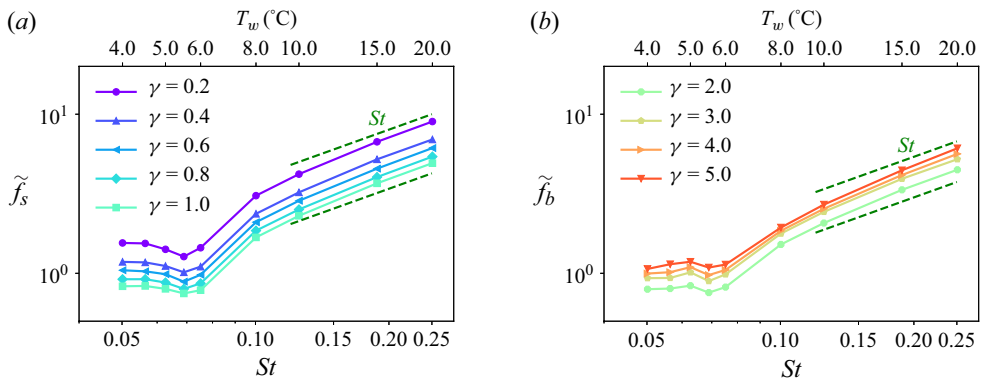


Figure 8. (a) The normalised side mean melt rate \tilde{f}_s as a function of the Stefan number St and the ambient temperature T_w in the side-melting dominant regime ($\gamma \leq 1$). (b) The normalised basal mean melt rate \tilde{f}_b as a function of the Stefan number St and the ambient temperature T_w in the basal-melting dominant regime ($\gamma \geq 2$).

melt rate \tilde{f}_b increases. Notably, \tilde{f}_s and \tilde{f}_b attain similar values at $\gamma \approx 1.5$. For $\gamma \leq 1$, \tilde{f}_s is larger than \tilde{f}_b , indicating a side-melting dominant regime. However, for $\gamma \geq 2$, \tilde{f}_b is larger than \tilde{f}_s , suggesting a basal-melting dominant regime. These observations are consistent with those for various Rayleigh numbers depicted in figure 2.

The normalised side mean melt rate \tilde{f}_s and the normalised basal mean melt rate \tilde{f}_b as a function of the Stefan number St and the ambient temperature T_w are shown in figure 8. When the ambient temperature is $T_w \geq 15^\circ\text{C}$, \tilde{f}_s and \tilde{f}_b follow the St scaling relation as indicated by (3.2). However, as the ambient temperature T_w decreases, the influence of the density anomaly intensifies, causing \tilde{f}_s and \tilde{f}_b to deviate from the St scaling relation. Notably, for $T_w \leq 8^\circ\text{C}$, \tilde{f}_s and \tilde{f}_b exhibit a non-monotonic dependence on the ambient temperature T_w : as the ambient temperature T_w decreases, \tilde{f}_s and \tilde{f}_b initially decrease,

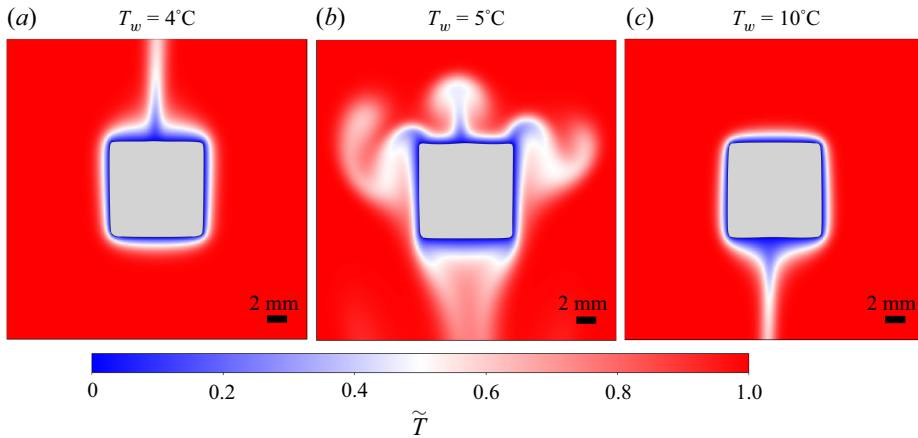


Figure 9. The instantaneous temperature field at time $t/t_m = 0.1$ for the ice block with aspect ratio $\gamma = 1.0$ for ambient temperature (a) $T_w = 4^\circ\text{C}$, (b) $T_w = 5^\circ\text{C}$ and (c) $T_w = 10^\circ\text{C}$ at $Ra = 1.46 \times 10^5$. Here, $\tilde{T} = T/T_w$. The dimensionless instantaneous heat fluxes Nu around the ice surface are 0.84, 0.63 and 0.84 in (a), (b) and (c), respectively.

reaching minimum values at $T_w \approx 5.5^\circ\text{C}$, and then slightly increase to larger values at $T_w \approx 4^\circ\text{C}$.

The non-monotonic behaviours of \tilde{f}_s and \tilde{f}_b arise from the density anomaly effect, which results in distinct flow structures at different ambient temperatures. Figure 9 shows the instantaneous temperature field for the ice block with aspect ratio $\gamma = 1.0$ for three different ambient temperatures at $Ra = 1.46 \times 10^5$. At low ambient temperatures (figure 9a), the meltwater ascends due to its density at 0°C being lower than that of the surrounding water. Conversely, at high ambient temperatures (figure 9c), the meltwater descends as its density exceeds that of the surrounding water. At intermediate ambient temperatures (figure 9b), a bi-directional flow pattern emerges: the meltwater initially moves upwards; as it mixes with and is warmed by the surrounding water, its density increases and becomes larger than that of the surrounding water, causing it to move downwards. This bi-directional flow pattern envelops the ice block, inhibiting the ambient warm water from directly contacting the ice, which results in a reduced dimensionless instantaneous heat flux Nu around the ice surface, and consequently slows down the melt rate. A similar bi-directional flow pattern was observed during the melting of an ice cylinder in 5.6°C fresh water (Weady *et al.* 2022) and the melting of an ellipsoid in 5.25°C fresh water (Yang *et al.* 2024a).

The normalised side mean melt rate \tilde{f}_s and the normalised basal mean melt rate \tilde{f}_b as a function of the aspect ratio γ for different ambient temperatures T_w are illustrated in figure 10. It is observed that for various ambient temperatures, the side mean melt rate \tilde{f}_s adheres to the $\gamma^{-3/8}$ scaling relation in the side-melting dominant regime ($\gamma \leq 1$), consistent with the scaling relation in (3.3). Similarly, the basal mean melt rate \tilde{f}_b follows the $\gamma^{3/8}$ scaling relation in the basal-melting dominant regime ($\gamma \geq 2$), which is consistent with the scaling relation in (3.4).

The compensated normalised overall mean melt rate \tilde{f}/St as function of γ for different ambient temperatures is shown in figure 11. The compensated normalised overall mean melt rate \tilde{f}/St at $T_w = 20^\circ\text{C}$ almost collapses with that at $T_w = 15^\circ\text{C}$, indicating that \tilde{f} follows the St scaling relation at $T_w \geq 15^\circ\text{C}$. However, as the ambient temperature T_w decreases, the density anomaly effect becomes stronger, and \tilde{f} no longer adheres to the St scaling relation. Moreover, the overall mean melt rate \tilde{f} exhibits a non-monotonic

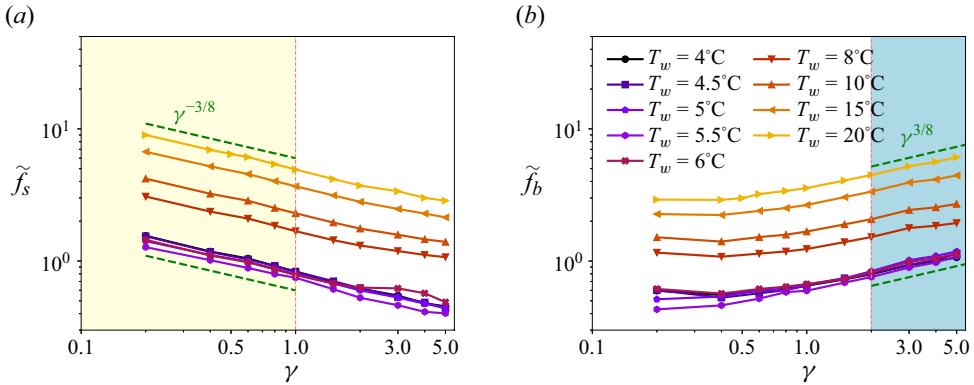


Figure 10. (a) The normalised side mean melt rate \tilde{f}_s as a function of the aspect ratio γ for different ambient temperatures T_w . (b) The normalised basal mean melt rate \tilde{f}_b as a function of the aspect ratio γ for different ambient temperatures T_w .

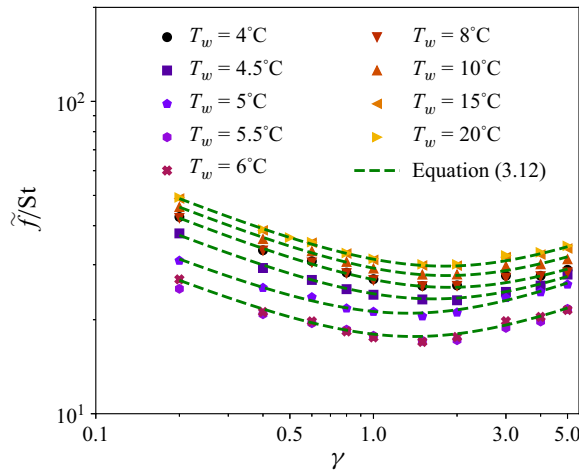


Figure 11. The compensated normalised overall mean melt rate \tilde{f}/St as a function of γ for different ambient temperatures. The symbols represent the compensated normalised overall mean melt rates \tilde{f}/St , while six green dashed lines represent the theoretical predictions from (3.12) for the overall mean melt rates \tilde{f}/St at $T_w = 4.5^\circ\text{C}$, 5°C , 6°C , 8°C , 10°C and 15°C , respectively.

dependence on the ambient temperature T_w : as the ambient temperature T_w decreases, the overall mean melt rate \tilde{f} initially decreases and then increases. These results are consistent with the behaviours of \tilde{f}_s and \tilde{f}_b for different ambient temperatures.

Furthermore, the normalised overall mean melt rate \tilde{f} for different ambient temperatures also exhibits a non-monotonic dependence on γ : as γ increases, \tilde{f} initially decreases and then increases. This non-monotonic behaviour is attributed to the competition between side and basal melting, similar to the observations for the overall mean melt rate \tilde{f} for different Rayleigh numbers (figure 6). It is observed that the minimum overall mean melt rate occurs at aspect ratio $\gamma_{min} \approx 2$ for both high ambient temperatures ($T_w > 6^\circ\text{C}$) and low ambient temperatures ($T_w < 5^\circ\text{C}$), corresponding to regimes of downward and upward flow, respectively. However, for intermediate temperatures ($5^\circ\text{C} \leq T_w \leq 6^\circ\text{C}$), γ_{min} decreases to approximately 1.5. This phenomenon can be explained as follows. For intermediate temperatures, a bi-directional flow pattern

emerges, characterised by both upward and downward flows. This bi-directional flow surrounds the ice block, insulating it from direct contact with the ambient warm water. Consequently, convection around the ice block weakens, and the influence of the perimeter length of the ice block becomes more significant. Therefore, for intermediate temperatures, γ_{min} shifts towards a value near $\gamma = 1$, where the perimeter of the square-shaped ice block is minimal.

The behaviours predicted by the theoretical model in (3.12) are also illustrated in figure 11. Six green dashed lines represent the theoretical predictions from (3.12) for the overall mean melt rates \tilde{f}/St at $T_w = 4.5^\circ\text{C}$, 5°C , 6°C , 8°C , 10°C and 15°C , respectively. The theoretical model in (3.12) captures the non-monotonic behaviour of \tilde{f} as function of γ , and accurately estimates the mean melt rate \tilde{f} across various ambient temperatures, particularly in the side-melting dominant regime ($\gamma \leq 1$) and the basal-melting dominant regime ($\gamma \geq 2$). This demonstrates that the theoretical model in (3.12) is also applicable for estimating the overall mean melt rate for different ambient temperatures.

It is noted that the influence of ambient temperature is examined only at relatively low Rayleigh numbers. This restriction arises because at low ambient temperatures, the melt rates are significantly slower, often several times lower than those observed at ambient temperature 20°C . Additionally, the time step required for simulating low-temperature cases is much smaller than that for 20°C , resulting in a substantially higher computational cost, particularly at high Rayleigh numbers. As a result, the effect of ambient temperature at higher Rayleigh numbers is not considered in the present study and is left for future investigation. Nevertheless, it can be anticipated that cavity formation persists at sufficiently high Rayleigh numbers, although the critical Rayleigh number for cavity formation at low ambient temperatures is expected to differ from that at 20°C . Furthermore, when the ambient temperature is very low (below 5°C), the density anomaly of water induces upward motion of the meltwater, leading to the cavity formation at the top surface of the ice block.

5. Conclusions and outlook

In this study, we have investigated the effect of the aspect ratio of an ice block with fixed volume (or area) on the side, basal and overall mean melt rates across a range of Rayleigh numbers and ambient temperatures through direct numerical simulations. Theoretical scaling relations and a model are proposed to estimate the side, basal and overall mean melt rates. They can describe the simulation results over the considered range of Rayleigh numbers and ambient temperatures.

The aspect ratio of the ice block has a significant effect on the relative contributions of side and basal melting. Specifically, the side mean melt rate \tilde{f}_s is larger than the basal mean melt rate \tilde{f}_b for aspect ratio $\gamma \leq 1$, while \tilde{f}_b exceeds \tilde{f}_s for $\gamma \geq 2$.

The influence of the Rayleigh number is first investigated for fixed ambient temperature $T_w = 20^\circ\text{C}$. The side mean melt rate \tilde{f}_s is found to follow a $Ra^{1/4}\gamma^{-3/8}$ scaling relation in the side-melting dominant regime ($\gamma \leq 1$) across different Rayleigh numbers. In contrast, the basal mean melt rate \tilde{f}_b exhibits a more complex behaviour: in the basal-melting dominant regime ($\gamma \geq 2$), \tilde{f}_b adheres to a $Ra^{1/4}\gamma^{3/8}$ scaling relation at low Rayleigh numbers ($Ra \leq 10^6$), but transitions to a $Ra^{1/3}\gamma^{1/2}$ scaling relation at high Rayleigh numbers ($Ra > 10^6$). This scaling transition is attributed to the formation of a bottom cavity caused by flow separation at high Rayleigh numbers, which enhances local mixing and subsequently increases the local melt rate. Furthermore, the overall mean melt rate \tilde{f} displays a non-monotonic dependence on the aspect ratio γ , initially decreasing and

then increasing as γ increases. This non-monotonic behaviour arises from the competition between side and basal melting. Based on the scaling relations for the side and basal mean melt rates, a theoretical model is proposed to also estimate the overall mean melt rate \tilde{f} . The proposed theoretical model successfully captures the non-monotonic behaviour of \tilde{f} , and also provides accurate predictions of \tilde{f} , especially in the regimes dominated by side melting ($\gamma \leq 0.8$) and basal melting ($\gamma \geq 3$).

Furthermore, the effect of ambient temperature is examined for fixed Rayleigh number $Ra = 1.46 \times 10^5$. The side, basal and overall mean melt rates follow the St scaling relation for the ambient temperature $T_w \geq 15^\circ\text{C}$. However, as the ambient temperature decreases further, the side, basal and overall mean melt rates deviate from the St scaling relation and exhibit a non-monotonic dependence on the ambient temperature, which is attributed to the density anomaly effect. Additionally, the proposed theoretical scaling relations and model are found to accurately predict the side, basal and overall mean melt rates for the analysed different ambient temperatures.

In summary, our findings provide insight into the role of the aspect ratio on side and basal melting of ice in freshwater. The proposed theoretical scaling relations and model may offer improved predictions of melt rates for ice blocks or icebergs with varying aspect ratios, and serve as a useful framework for refining large-scale geophysical models. It is, however, important to note that the Rayleigh number range considered in this study is considerably lower than that observed at geophysical scales. The applicability of the proposed scaling relations for the side and basal melt rates to geophysical scales remains to be verified. Nonetheless, the methodology for estimating the overall melt rate based on the side and basal melt rates can be extended to geophysical icebergs. In future studies, it would be worthwhile to further explore additional factors such as the influence of salinity, mean shear from the ambient flow, and spatial variations in the temperature along the ice surface.

Movies depicting the instantaneous fields corresponding to the cases presented in figures 5 and 9 are provided in the supplementary material. The solver is available at <https://github.com/chowland/AFiD-MuRPhFi>. Mean statistics for the cases in the present study are available at <https://doi.org/10.5281/zenodo.14589263>.

Supplementary movies. Supplementary movies are available at <https://doi.org/10.1017/jfm.2025.302>.

Funding. This work was financially supported by the European Union (ERC, MultiMelt, 101094492). We also acknowledge the EuroHPC Joint Undertaking for awarding the project EHPC-REG-2023R03-178 access to the EuroHPC supercomputer Discoverer, hosted by Sofia Tech Park (Bulgaria).

Declaration of interests. The authors report no conflict of interest.

Appendix A. The influence of the computational domain size and the grid convergence test of the simulations

The influence of the computational domain size is analysed for the 2-D case with $Ra = 1.82 \times 10^4$, $\gamma = 1.0$ and $St = 0.25$, as shown in figure 12(a). The normalised overall mean melt rate \tilde{f} exhibits convergence as the ratio L/D of the box size L to the effective length D of the ice block increases, which indicates that the impact of the side walls on \tilde{f} becomes negligible when $L/D \geq 8$. Based on this observation, the domain size is selected as $L/D = 10$ for the present study.

Grid convergence tests were conducted for multiple cases to ensure convergent results. For brevity, we present only the grid-independence test for the 2-D case with $Ra = 1.82 \times 10^4$, $\gamma = 1.0$ and $St = 0.25$ in figure 12(b–d). The results exhibit convergence

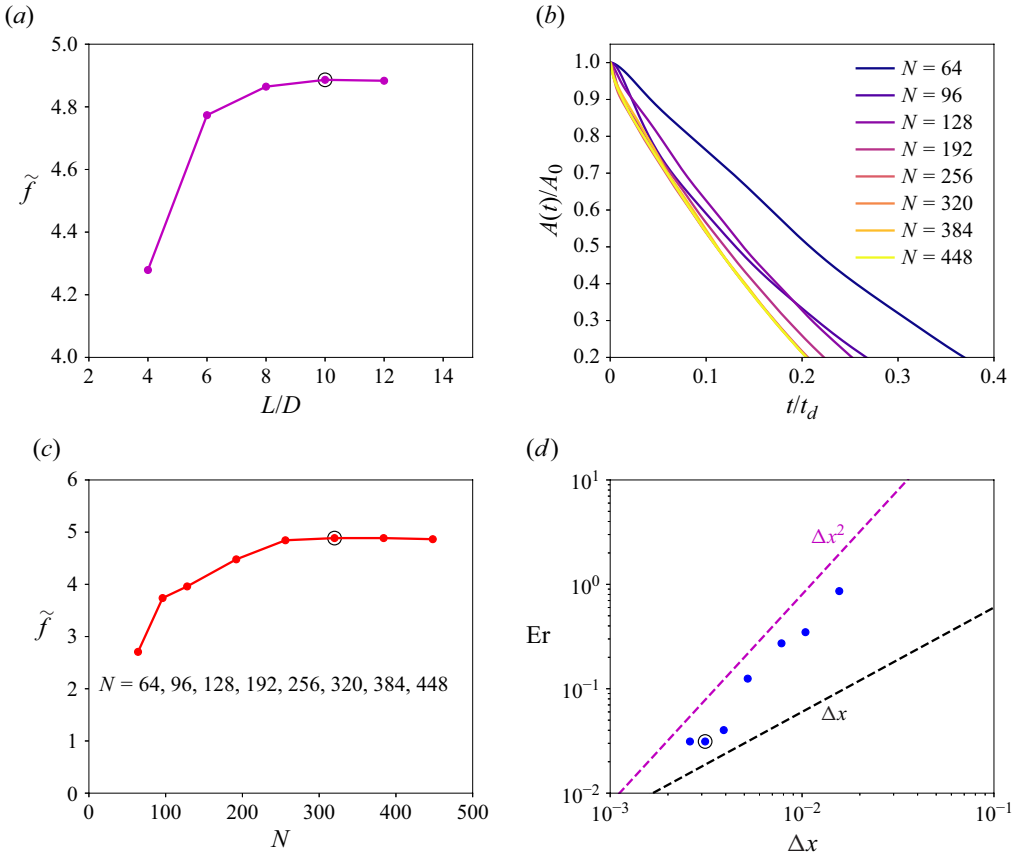


Figure 12. (a) The normalised overall mean melt rate \tilde{f} as a function of the ratio L/D of the box size L to the effective length D of the ice block for the 2-D case with $Ra = 1.82 \times 10^4$, $\gamma = 1.0$ and $St = 0.25$. The domain size is chosen as $L/D = 10$, as indicated by the black circle. (b) The normalised area of ice $A(t)/A_0$ as a function of time t/t_d for the 2-D case with $Ra = 1.82 \times 10^4$, $\gamma = 1.0$ and $St = 0.25$. Here, A_0 is the initial area of the ice block. (c) The normalised overall mean melt rate \tilde{f} as a function of the grid resolution N for the velocity and temperature fields. Convergence is observed with increasing N , and the resolution $N = 320$ was selected, as denoted by the black circle. (d) The relative error $Er = |t_m - t_{m0}|/t_{m0}$ as a function of the grid spacing Δx , where t_{m0} is the melt time t_m for the highest resolution. The selected grid resolution is highlighted by the black circle.

with increasing grid resolution. Consequently, we selected $N = 320$ as the grid resolution for our simulations, as indicated by the black circle in figure 12(c).

Appendix B. The temporal evolutions of the equivalent aspect ratio and the side and basal melt rates

The temporal evolutions of the equivalent aspect ratio $\gamma(t)$ as well as the side and basal melt rates $\tilde{f}_s(t)$ and $\tilde{f}_b(t)$ for various initial aspect ratios γ at $Ra = 1.17 \times 10^6$ are presented in figure 13. Additionally, figure 14 illustrates the evolutions of the normalised instantaneous side and basal melt rates, $\tilde{f}_s(t)/\gamma^{-3/8}$ and $\tilde{f}_b(t)/\gamma^{3/8}$, as functions of the normalised instantaneous equivalent aspect ratio $\gamma(t)/\gamma$ at the same Rayleigh number. Similar trends are observed for cases with different Rayleigh numbers and ambient temperatures, and are omitted here for brevity.

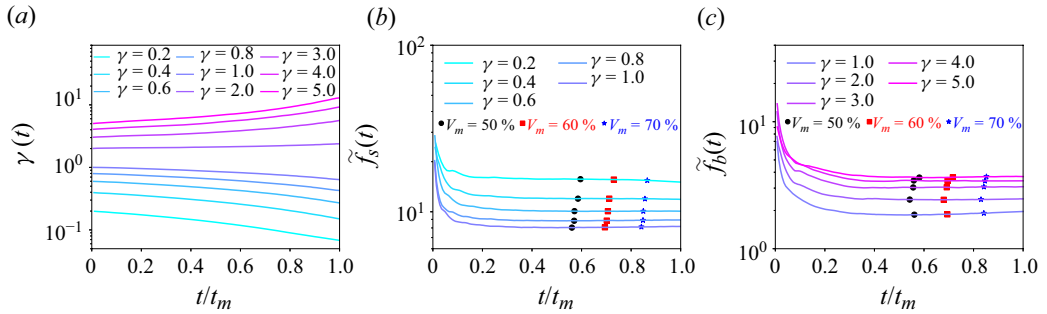


Figure 13. (a) The temporal evolution of the instantaneous equivalent aspect ratio $\gamma(t)$ for various initial aspect ratios γ at $Ra = 1.17 \times 10^6$, where $\gamma(t) = w(t)/h(t)$. (b) The temporal evolution of the instantaneous side melt rate $\tilde{f}_s(t)$ for various initial aspect ratios $\gamma \leq 1$ at $Ra = 1.17 \times 10^6$. (c) The temporal evolution of the instantaneous basal melt rate $\tilde{f}_b(t)$ for various initial aspect ratios $\gamma \geq 1$ at $Ra = 1.17 \times 10^6$. Here, t_m denotes the time required to melt $V_m = 80\%$ of the initial area in 2-D simulations, and $t/t_m = 1.0$ represents the time at which 80% of the initial area has melted. Furthermore, the black filled circle, red square and blue star correspond to the times required to melt 50%, 60% and 70% of the initial area, respectively, as shown in (b) and (c).

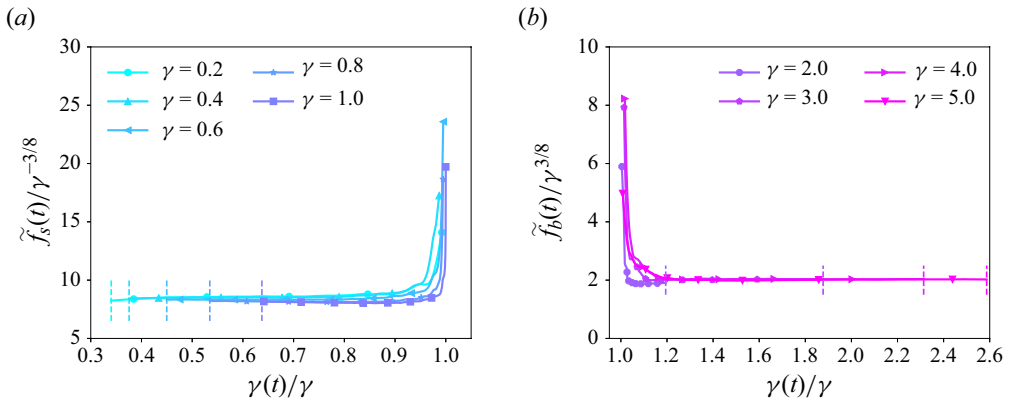


Figure 14. (a) The temporal evolution of the normalised instantaneous side melt rate $\tilde{f}_s(t)/\gamma^{-3/8}$ for various initial aspect ratios $\gamma \leq 1$ as a function of the normalised instantaneous equivalent aspect ratio $\gamma(t)/\gamma$ at $Ra = 1.17 \times 10^6$. (b) The temporal evolution of the normalised instantaneous basal melt rate $\tilde{f}_b(t)/\gamma^{3/8}$ for various initial aspect ratios $\gamma \geq 2$ as a function of the normalised instantaneous equivalent aspect ratio $\gamma(t)/\gamma$ at $Ra = 1.17 \times 10^6$. In both plots, the vertical dashed lines indicate the values of $\gamma(t)/\gamma$ at the melt time t_m .

As shown in figure 13(a), the equivalent aspect ratio $\gamma(t)$ is changing over time, with a gradual decrease for initial aspect ratio $\gamma \leq 1$, and a gradual increase for $\gamma \geq 2$. This phenomenon can be attributed to the relative magnitudes of the side and basal mean melt rates. For the cases with initial aspect ratio $\gamma \leq 1$, figure 2 demonstrates that the side mean melt rate \tilde{f}_s exceeds the basal mean melt rate \tilde{f}_b , leading to a progressive reduction in $\gamma(t)$ as the ice melts. Furthermore, figure 14(a) indicates that the range of the normalised instantaneous equivalent aspect ratio $\gamma(t)/\gamma$ increases as the initial aspect ratio γ decreases. This can be explained by the trend observed in figure 2, where the difference between \tilde{f}_s and \tilde{f}_b becomes more pronounced as γ decreases.

Conversely, for cases with $\gamma \geq 2$, figure 2 reveals that the basal mean melt rate \tilde{f}_b is larger than the side mean melt rate \tilde{f}_s , resulting in a gradual increase in $\gamma(t)$. Moreover, figure 14(b) shows that the range of $\gamma(t)/\gamma$ increases as γ increases, which can be

attributed to the increasing disparity between \tilde{f}_b and \tilde{f}_s as γ increases, as depicted in figure 2.

The temporal evolutions of the side and basal melt rates $\tilde{f}_s(t)$ and $\tilde{f}_b(t)$ exhibit similar trends. Initially, both melt rates are relatively large due to the higher temperature gradients near the ice surface. Then the side and basal melt rates $\tilde{f}_s(t)$ and $\tilde{f}_b(t)$ gradually decrease, reaching nearly constant values as the ice continues to melt. Both $\tilde{f}_s(t)$ and $\tilde{f}_b(t)$ are almost constant over time, particularly within the range $60\% \leq V_m \leq 80\%$. It is noted that the influence of the initial condition becomes less significant as the final melt fraction V_m increases. Consequently, a larger value of V_m is preferable to effectively mitigate the effect of the initial condition. However, the final melt fraction V_m cannot be excessively large, as the ice block may fracture into two pieces when $V_m \approx 90\%$, particularly under high Rayleigh number and large aspect ratio conditions. Thus a final melt fraction $V_m = 80\%$ is chosen in the present study to significantly reduce the impact of the initial condition.

Figure 14 demonstrates that the normalised instantaneous side melt rate $\tilde{f}_s(t)/\gamma^{-3/8}$ for initial aspect ratios $\gamma \leq 1$ and the normalised instantaneous basal melt rate $\tilde{f}_b(t)/\gamma^{3/8}$ for initial aspect ratios $\gamma \geq 2$ nearly collapse respectively, particularly within the range $60\% \leq V_m \leq 80\%$. This suggests that despite the temporal evolution of the equivalent aspect ratio $\gamma(t)$ deviating from its initial value γ , the proposed scaling relations in the present study remain valid for the instantaneous side melt rate $\tilde{f}_s(t)$ in the side-melting dominant regime ($\gamma \leq 1$), and for the instantaneous basal melt rate $\tilde{f}_b(t)$ in the basal-melting dominant regime ($\gamma \geq 2$).

However, it is important to note that the variation in the instantaneous equivalent aspect ratio $\gamma(t)$ is relatively large, particularly for cases with small or large initial aspect ratios. The substantial departure of $\gamma(t)$ from its initial value γ results in the breakdown of the proposed scaling relations for predicting the side melt rate \tilde{f}_s in the basal-melting dominant regime ($\gamma \geq 2$), and the basal melt rate \tilde{f}_b in the side-melting dominant regime ($\gamma \leq 1$), as illustrated in figures 3(c) and 4(c). Consequently, these discrepancies also impact the accuracy of estimating the overall mean melt rate \tilde{f} using the proposed scaling relations for \tilde{f}_s and \tilde{f}_b .

To improve the predictive capability of the scaling relations for \tilde{f}_s in the basal-melting dominant regime, \tilde{f}_b in the side-melting dominant regime, and the overall mean melt rate \tilde{f} , future studies should account for the temporal evolution of the equivalent aspect ratio.

REFERENCES

- AHLERS, G., GROSSMANN, S. & LOHSE, D. 2009 Heat transfer and large scale dynamics in turbulent Rayleigh–Bénard convection. *Rev. Mod. Phys.* **81** (2), 503–537.
- ANDRES, M., SILVANO, A., STRANEO, F. & WATTS, D.R. 2015 Icebergs and sea ice detected with inverted echosounders. *J. Atmos. Ocean. Technol.* **32** (5), 1042–1057.
- BEJAN, A. 1993 *Heat Transfer*. Wiley.
- BUDD, W.F., JACKA, T.H. & MORGAN, V.I. 1980 Antarctic iceberg melt rates derived from size distributions and movement rates. *Ann. Glaciol.* **1**, 103–112.
- CENEDESE, C. & STRANEO, F. 2023 Icebergs melting. *Annu. Rev. Fluid Mech.* **55** (1), 377–402.
- CHEN, J.L., WILSON, C.R. & TAPLEY, B.D. 2006 Satellite gravity measurements confirm accelerated melting of Greenland ice sheet. *Science* **313** (5795), 1958–1960.
- COUSTON, L.-A., HESTER, E., FAVIER, B., TAYLOR, J.R., HOLLAND, P.R. & JENKINS, A. 2021 Topography generation by melting and freezing in a turbulent shear flow. *J. Fluid Mech.* **911**, A44.
- DAVIS, S.H., MÜLLER, U. & DIETSCHKE, C. 1984 Pattern selection in single-component systems coupling Bénard convection and solidification. *J. Fluid Mech.* **144**, 133–151.
- DHAIDAN, N.S. & KHODADADI, J. 2015 Melting and convection of phase change materials in different shape containers: a review. *Renew. Sustain. Energy Rev.* **43**, 449–477.
- DIETSCHKE, C. & MÜLLER, U. 1985 Influence of Bénard convection on solid–liquid interfaces. *J. Fluid Mech.* **161**, 249–268.

- DU, Y., CALZAVARINI, E. & SUN, C. 2024 The physics of freezing and melting in the presence of flows. *Nat. Rev. Phys.* **6** (11), 676–690.
- DUPRAT, L., BIGG, G. & WILTON, D. 2016 Enhanced Southern Ocean marine productivity due to fertilization by giant icebergs. *Nat. Geosci.* **9** (3), 219–221.
- DUTRIEUX, P., STEWART, C., JENKINS, A., NICHOLLS, K.W., CORR, H.F.J., RIGNOT, E. & STEFFEN, K. 2014 Basal terraces on melting ice shelves. *Geophys. Res. Lett.* **41** (15), 5506–5513.
- EPSTEIN, M. & CHEUNG, F.B. 1983 Complex freezing–melting interfaces in fluid flow. *Annu. Rev. Fluid Mech.* **15** (1), 293–319.
- FAVIER, B., PURSEED, J. & DUCHEMIN, L. 2019 Rayleigh–Bénard convection with a melting boundary. *J. Fluid Mech.* **858**, 437–473.
- GEBHART, B. & MOLLENDORF, J.C. 1977 A new density relation for pure and saline water. *Deep Sea Res.* **24** (9), 831–848.
- GROSSMANN, S. & LOHSE, D. 2000 Scaling in thermal convection: a unifying theory. *J. Fluid Mech.* **407**, 27–56.
- GROSSMANN, S. & LOHSE, D. 2001 Thermal convection for large Prandtl numbers. *Phys. Rev. Lett.* **86** (15), 3316–3319.
- HAO, Y.L. & TAO, Y.X. 2002 Heat transfer characteristics of melting ice spheres under forced and mixed convection. *J. Heat Transfer* **124** (5), 891–903.
- HESTER, E.W., COUSTON, L.-A., FAVIER, B., BURNS, K.J. & VASIL, G.M. 2020 Improved phase-field models of melting and dissolution in multi-component flows. *Proc. R. Soc. Lond. A: Math. Phys. Engng Sci.* **476** (2242), 20200508.
- HESTER, E.W., MCCONNOCHIE, C.D., CENEDESE, C., COUSTON, L.-A. & VASIL, G. 2021 Aspect ratio affects iceberg melting. *Phys. Rev. Fluids* **6** (2), 023802.
- HOLMAN, J.P. 2010 *Heat Transfer*. 10th edn. McGraw-Hill.
- HOWLAND, C.J. 2022 AFiD-MuRPhFi documentation. Available at <https://chowland.github.io/AFiD-MuRPhFi/>.
- HUPPERT, H.E. & TURNER, J.S. 1978 On melting icebergs. *Nature* **271** (5640), 46–48.
- JENKINS, M. & DAI, A. 2021 The impact of sea-ice loss on Arctic climate feedbacks and their role for Arctic amplification. *Geophys. Res. Lett.* **48** (15), e2021GL094599.
- KADANOFF, L.P. 2001 Turbulent heat flow: structures and scaling. *Phys. Today* **54** (8), 34–39.
- LIU, H.R., NG, C.S., CHONG, K.L., LOHSE, D. & VERZICCO, R. 2021 An efficient phase-field method for turbulent multiphase flows. *J. Comput. Phys.* **446**, 110659.
- LOHSE, D. & SHISHKINA, O. 2023 Ultimate turbulent thermal convection. *Phys. Today* **76** (11), 26–32.
- LOHSE, D. & SHISHKINA, O. 2024 Ultimate Rayleigh–Bénard turbulence. *Rev. Mod. Phys.* **96** (3), 035001.
- LOHSE, D. & XIA, K. 2010 Small-scale properties of turbulent Rayleigh–Bénard convection. *Annu. Rev. Fluid Mech.* **42** (1), 335–364.
- MALYARENKO, A., WELLS, A.J., LANGHORNE, P.J., ROBINSON, N.J., WILLIAMS, M.J. & NICHOLLS, K.W. 2020 A synthesis of thermodynamic ablation at ice–ocean interfaces from theory, observations and models. *Ocean Model.* **154**, 101692.
- MARTIN, T. & ADCROFT, A. 2010 Parameterizing the fresh-water flux from land ice to ocean with interactive icebergs in a coupled climate model. *Ocean Model.* **34** (3–4), 111–124.
- OSTILLA-MÓNICO, R., YANG, Y., VAN DER POEL, E.P., LOHSE, D. & VERZICCO, R. 2015 A multiple-resolution strategy for direct numerical simulation of scalar turbulence. *J. Comput. Phys.* **301**, 308–321.
- PISTONE, K., EISENMAN, I. & RAMANATHAN, V. 2014 Observational determination of albedo decrease caused by vanishing Arctic sea ice. *Proc. Natl Acad. Sci. USA* **111** (9), 3322–3326.
- VAN DER POEL, E.P., OSTILLA-MÓNICO, R., DONNERS, J. & VERZICCO, R. 2015 A pencil distributed finite difference code for strongly turbulent wall-bounded flows. *Comput. Fluids* **116**, 10–16.
- RACKOW, T., WESCHE, C., TIMMERMANN, R., HELLMER, H.H., JURICKE, S. & JUNG, T. 2017 A simulation of small to giant Antarctic iceberg evolution: differential impact on climatology estimates. *J. Geophys. Res. Oceans* **122** (4), 3170–3190.
- RAHMAN, M.S. 2020 *Handbook of Food Preservation*. 3rd edn. CRC Press.
- RAVICHANDRAN, S., TOPPALADODDI, S. & WETTLAUER, J.S. 2022 The combined effects of buoyancy, rotation, and shear on phase boundary evolution. *J. Fluid Mech.* **941**, A39.
- RAVICHANDRAN, S. & WETTLAUER, J.S. 2021 Melting driven by rotating Rayleigh–Bénard convection. *J. Fluid Mech.* **916**, A28.
- RISTROPH, L. 2018 Sculpting with flow. *J. Fluid Mech.* **838**, 1–4.
- RUBINSTEIN, L. 1971 *The Stefan Problem*. American Mathematical Society.
- SCHLICHTING, H. & GERSTEN, K. 2017 *Boundary Layer Theory*. Springer.

- SILVA, T.A.M., BIGG, G.R. & NICHOLLS, K.W. 2006 Contribution of giant icebergs to the Southern Ocean freshwater flux. *J. Geophys. Res.* **111** (C3), C03004.
- SMITH, K.L., SHERMAN, A.D., SHAW, T.J. & SPRINTALL, J. 2013 Icebergs as unique Lagrangian ecosystems in polar seas. *Annu. Rev. Mar. Sci.* **5** (1), 269–287.
- SROKOSZ, M., BARINGER, M., BRYDEN, H., CUNNINGHAM, S., DELWORTH, T., LOZIER, S., MAROTZKE, J. & SUTTON, R. 2012 Past, present, and future changes in the Atlantic meridional overturning circulation. *Bull. Am. Meteor. Soc.* **93** (11), 1663–1676.
- SUTHERLAND, D.A., JACKSON, R.H., KIENHOLZ, C., AMUNDSON, J.M., DRYER, W.P., DUNCAN, D., EIDAM, E.F., MOTYKA, R.J. & NASH, J.D. 2019 Direct observations of submarine melt and subsurface geometry at a tidewater glacier. *Science* **365** (6451), 369–374.
- TOPPALADODDI, S. 2021 Nonlinear interactions between an unstably stratified shear flow and a phase boundary. *J. Fluid Mech.* **919**, A28.
- TRUFFER, M. & MOTYKA, R.J. 2016 Where glaciers meet water: subaqueous melt and its relevance to glaciers in various settings. *Rev. Geophys.* **54** (1), 220–239.
- VANIER, C.R. & TIEN, C. 1970 Free convection melting of ice spheres. *AIChE J.* **16** (1), 76–82.
- VERZICCO, R. & ORLANDI, P. 1996 A finite-difference scheme for three-dimensional incompressible flows in cylindrical coordinates. *J. Comput. Phys.* **123** (2), 402–414.
- WANG, Z., CALZAVARINI, E., SUN, C. & TOSCHI, F. 2021a How the growth of ice depends on the fluid dynamics underneath. *Proc. Natl Acad. Sci. USA* **118** (10), 10.
- WANG, Z., JIANG, L., DU, Y., SUN, C. & CALZAVARINI, E. 2021b Ice front shaping by upward convective current. *Phys. Rev. Fluids* **6** (9), L091501.
- WEADY, S., TONG, J., ZIDOVSKA, A. & RISTROPH, L. 2022 Anomalous convective flows carve pinnacles and scallops in melting ice. *Phys. Rev. Lett.* **128** (4), 044502.
- WEEKS, W.F. & CAMPBELL, W.J. 1973 Icebergs as a fresh-water source: an appraisal. *J. Glaciol.* **12** (65), 207–233.
- YANG, R., VAN DEN HAM, T., VERZICCO, R., LOHSE, D. & HUISMAN, S. 2024a Circular objects do not melt the slowest in water. *Phys. Rev. Fluids* **9** (8), 083501.
- YANG, R., HOWLAND, C.J., LIU, H.-R., VERZICCO, R. & LOHSE, D. 2023 Morphology evolution of a melting solid layer above its melt heated from below. *J. Fluid Mech.* **956**, A23.
- YANG, R., HOWLAND, C.J., LIU, H.-R., VERZICCO, R. & LOHSE, D. 2024b Shape effect on solid melting in flowing liquid. *J. Fluid Mech.* **980**, R1.